

Article

Microwave-Solvothermal Synthesis of Mesoporous CeO₂/CNCs Nanocomposite for Enhanced Room Temperature NO₂ Detection

Yanming Sun ^{1,*} , Xiaoying Lu ² , Yanchen Huang ² and Guoping Wang ¹

¹ College of Electronics and Information Engineering, Shenzhen University, 3688 Nanhai Boulevard, Shenzhen 518060, China; gpwang@szu.edu.cn

² Institute of Microscale Optoelectronics, Shenzhen University, Shenzhen 518060, China; luxiaoying9915@163.com (X.L.); 13677042086@163.com (Y.H.)

* Correspondence: sunym@szu.edu.cn

Abstract: Nitrogen dioxide (NO₂) gas sensors are pivotal in upholding environmental integrity and human health, necessitating heightened sensitivity and exceptional selectivity. Despite the prevalent use of metal oxide semiconductors (MOSs) for NO₂ detection, extant solutions exhibit shortcomings in meeting practical application criteria, specifically in response, selectivity, and operational temperatures. Here, we successfully employed a facile microwave-solvothermal method to synthesize a mesoporous CeO₂/CNCs nanocomposite. This methodology entails the rapid and comprehensive dispersion of CeO₂ nanoparticles onto helical carbon nanocoils (CNCs), resulting in augmented electronic conductivity and an abundance of active sites within the composite. Consequently, the gas-sensing sensitivity of the nanocomposite at room temperature experienced a notable enhancement. Moreover, the presence of cerium oxide and the conversion of Ce³⁺ and Ce⁴⁺ ions facilitated the generation of oxygen vacancies in the composites, thereby further amplifying the sensing performance. Experimental outcomes demonstrate that the nanocomposite exhibited an approximate 9-fold increase in response to 50 ppm NO₂ in comparison to pure CNCs at room temperature. Additionally, the CeO₂/CNCs sensor displayed remarkable selectivity towards NO₂ when exposed to gases such as NH₃, CO, SO₂, CO₂, and C₂H₅OH. This straightforward microwave-solvothermal method presents an appealing strategy for the research and development of intelligent sensors based on CNCs nanomaterials.



Citation: Sun, Y.; Lu, X.; Huang, Y.; Wang, G. Microwave-Solvothermal Synthesis of Mesoporous CeO₂/CNCs Nanocomposite for Enhanced Room Temperature NO₂ Detection. *Nanomaterials* **2024**, *14*, 812. <https://doi.org/10.3390/nano14100812>

Academic Editor: Jose Maria Calderon-Moreno

Received: 10 April 2024

Revised: 25 April 2024

Accepted: 30 April 2024

Published: 7 May 2024



Copyright: © 2024 by the authors. Licensee MDPI, Basel, Switzerland. This article is an open access article distributed under the terms and conditions of the Creative Commons Attribution (CC BY) license (<https://creativecommons.org/licenses/by/4.0/>).

Keywords: microwave-solvothermal method; CeO₂/CNCs nanocomposite; gas-sensing; oxygen vacancies

1. Introduction

Over the past few decades, the escalating emission of nitrogen oxides (NO_x), particularly nitrogen dioxide (NO₂) stemming from industrial fuel combustion and vehicle exhaust, has posed an increasingly severe threat to the environment and human health. Prolonged exposure to NO₂ not only has detrimental effects on the respiratory system, heightening the risk of mycoplasma respiratory infections, asthma, and pneumonia [1,2], but is also a major contributor to acid rain formation, causing damage to crops and environmental contamination [3]. Consequently, there is an urgent need for the development of an efficient nitrogen dioxide gas sensor. Chemoresistive gas sensors, particularly those based on Metal-Oxide-Semiconductor (MOS) technology, have attracted considerable attention in the field of gas sensing. This is primarily due to their simple structure, ease of preparation, and cost effectiveness [4]. MOS-based gas sensors demonstrate exceptional selectivity and sensitivity to specific gases, attributable to their distinctive micro-/nanoscale structure and morphology [5]. Both p-type MOS (such as Co₃O₄ [6], CuO [7], NiO [8]) and n-type MOS (such as ZnO [9], TiO₂ [10], Al₂O₃ [11]) have been extensively investigated for sensing applications. Ceria (CeO₂), characterized as a semiconductor material with a wide bandgap (3.2 eV), holds significant promise across various fields, including energy

storage devices [12], magnetic wave absorbers [13], and photocatalytic applications [14]. Furthermore, ceria emerges as a potentially economical nanomaterial for gas sensing due to its chemical stability, mixed valence, and high oxygen absorption capacity [15]. Researchers have also explored the use of doped ceria with metal/metal oxide, which has shown fast response times and high selectivity [16,17]. However, the intrinsic low conductivity of ceria mandates high-temperature operation, thereby restricting its practical applications. It is crucial to identify a suitable material for modifying the properties of cerium oxide to enable detection at room temperature (RT).

In recent years, extensive research has been conducted on carbon nanomaterials due to their remarkable ability to transport electrons, immense surface area, and excellent electrical conductivity. Carbon nanotubes (CNTs), graphene oxide (GO) and reduced graphene oxide (rGO) have emerged as promising materials for toxic gas detection at RT, benefiting from their myriad functional groups and superior conductive network [18–21]. Nevertheless, their limited selectivity and prolonged reaction times have impeded their widespread utilization in gas sensors. To tackle this challenge, a potential solution involves integrating metal semiconductors with carbon materials to enhance both gas adsorption and electrical conductivity. For instance, Liu et al. [22] synthesized a ZnO/rGO nanocomposite through a thermal reduction and soft solution process, showcasing a heightened response and shorter response-recovery behavior compared to a pure ZnO sensor when employed as a nitrogen dioxide sensor at RT. Nonetheless, the multilayer stacking overlap of graphene oxide nanosheets in this composite failed to provide sufficient active sites, resulting in diminished sensing sensitivity. Therefore, there remains a necessity to identify an alternative nanostructured material possessing both a large specific surface area and an abundance of active sites for effective adsorption of target gases.

The as-grown carbon nanocoils (CNCs), comprised of coiled carbon nanotubes (CNTs) connected by amorphous carbon nanofibers (CNFs), represent a distinctive structural configuration [23,24]. Characterized by a unique helical structure amalgamating sp^2 grains and sp^3 amorphous structures [23], CNCs exhibit physical properties that set them apart from both CNTs and CNFs [24]. This spiral polycrystalline-amorphous nature renders CNCs highly advantageous for a spectrum of applications, including field-emission devices, electromagnetic wave absorbers, humidity sensors, and acoustic sensors [25–28]. Moreover, the helical architecture of CNCs contributes to an augmented surface area, facilitating gas molecule adsorption by providing an abundance of active sites. CNCs have demonstrated promising potential as active materials in gas sensing applications. For example, a NO_2 sensor based on CNCs decorated with NiO nanosheets has been developed using a hydrothermal method. This sensor has a detection concentration limit of 60.3 ppb and demonstrates selectivity towards NO_2 at RT [29]. However, it should be noted that this sensor requires a lengthy hydrothermal reaction time and exhibits a relatively subdued response.

In this study, we propose a rapid and straightforward microwave-solvothermal (MWS) method for synthesizing CeO_2 /CNCs nanocomposites with a mesoporous structure, achieved by embellishing CNCs with CeO_2 nanoparticles. The nanoparticles produced through the MWS method demonstrate characteristics of a narrow particle size distribution, minimal agglomeration, and uniform morphology [30,31]. In this way, the crystalline CeO_2 nanoparticles can be evenly anchored onto the chemical vapor deposition (CVD)-grown CNCs in a short period. Furthermore, the as-obtained CeO_2 /CNCs composites exhibit a mesoporous structure and helical morphology, thereby providing a greater number of exposed active sites and larger specific surface areas for the adsorption and diffusion of gas molecules. Additionally, the exceptional conductivity of CNCs facilitates the establishment of a complete electric conduction network, reducing the operational resistance of the original CeO_2 and improving its detection capabilities at room temperature. Moreover, the electron hopping within the helical CNCs contributes to the efficient transport of charge carriers, resulting in an elevated signal level [24]. Simultaneously, the composite exhibits a significant presence of oxygen vacancies, further contributing to its exceptional redox

capacity. As a result, the CeO_2/CNCs nanocomposites demonstrate high sensitivity and exceptional selectivity in detecting NO_2 at RT. The facile synthesis of CeO_2/CNCs composites using the microwave-solvothermal approach represents an innovative and promising avenue for the development of low-temperature nitrogen dioxide-sensing materials.

2. Experiments

2.1. Synthesis of CNCs and CeO_2/CNCs Nanocomposite

A large amount of CNCs were prepared via a CVD process with catalyst of Fe/Sn [23,24]. Specifically, the mole ratio of Fe to Sn in the $\text{Fe}(\text{NO}_3)_3/\text{SnCl}_4$ precursor solution was controlled to be 60:1. The CNCs were synthesized by using a thermal CVD technology at 720°C for 4 h with introducing 30 and 300 sccm of C_2H_2 and Ar gases, respectively. Then, the obtained CNC clusters were refined for additional processing by being dissolved in ethanol solution using an ultrasonic device for 30 s, thereafter collected the purified CNC samples from supernatant to remove impurity particles.

The synthesis of the CeO_2/CNCs nanocomposite was carried out using a microwave-solvothermal method, as illustrated in Figure 1a. Initially, 20 mg of CNCs functionalized by acid solution ($\text{HNO}_3:\text{H}_2\text{SO}_4$ in 1:3 (*v/v*) ratio) were dispersed in 20 mL of N,N-dimethylformamide (DMF) and subjected to sonication for 30 min. Subsequently, 0.7 g of cerous nitrate hexahydrate ($\text{Ce}(\text{NO}_3)_3 \cdot 6\text{H}_2\text{O}$) was dissolved in 20 mL of anhydrous ethanol and sonicated for 30 min. Then, the $\text{Ce}(\text{NO}_3)_3$ solution was added dropwise to the previous solution while continuously stirring magnetically for 1 h. After that, the as-prepared solution was shifted to a 50 mL autoclave, and subsequently treated under a microwave system (microwave 600 W) at 140°C for 1 h. After naturally cooling to room temperature, the precipitate was collected, washed with deionized water and pure ethanol, and dried at 60°C for 12 h. Finally, the obtained powders were calcined at 300°C under vacuum conditions for 2 h, resulting in the formation of CeO_2/CNCs nanocomposites.

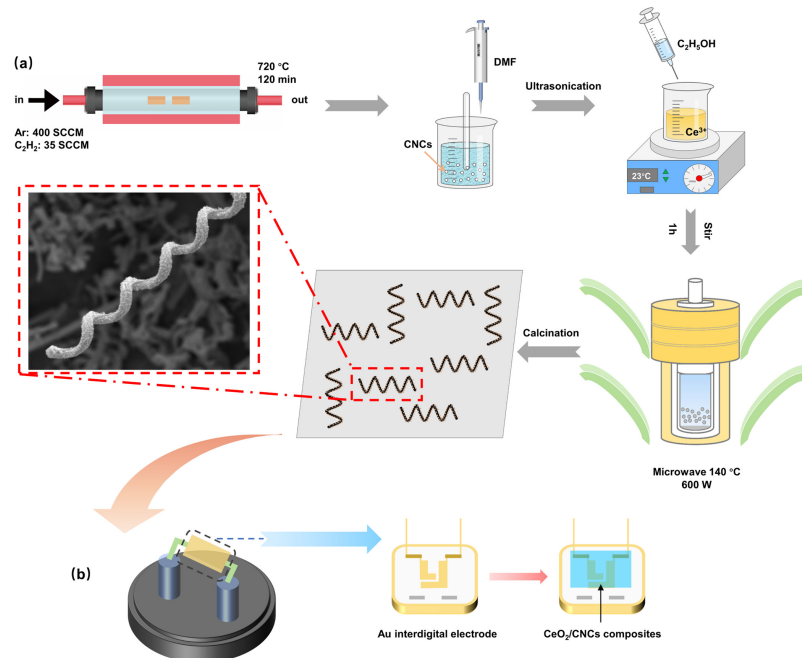


Figure 1. Schematic representation of (a) the synthesis process of CeO_2/CNCs nanocomposites; (b) fabrication of gas sensor.

In order to conduct a comparative analysis, we obtained samples containing varying amounts of cerous nitrate hexahydrate (0.3 g, 0.5 g, 0.7 g, and 0.9 g). These samples were designated as CeO_2/CNCs -0.3, CeO_2/CNCs -0.5, CeO_2/CNCs -0.7, and CeO_2/CNCs -0.9, respectively. Furthermore, employing similar parameters, we synthesized nanocomposites with different compositions by manipulating the temperature of the solvent thermal

reaction (100 °C, 120 °C, 140 °C, and 160 °C), and labeled them as sample 1, sample 2, sample 3 and sample 4, respectively. Additionally, for the purpose of further comparison, we prepared bare CNCs under identical experimental conditions.

2.2. Characterization

X-ray diffraction radiation (XRD, MiniFlex600, Rigaku) was used to determine the crystallographic phase of the as-prepared samples, with a CuK α radiation in the range from 10° to 85°. The Raman spectra patterns were acquired on a Raman spectrometer in the energy range of 200–2000 cm⁻¹, the laser utilized to record with an excitation source of 638 nm. Field-emission scanning electron microscope (FE-SEM, FEI Scios, Germany) was used to investigate the morphological characteristics. The TEM images were taken using a JEOL 2200FS electronic microscope operating at 200 kV. The surface area and the pore size were estimated by N₂ adsorption–desorption isotherms using an ASAP 2460 (Micromeritics, USA). The specific surface area of the samples was calculated based on the multi-point adsorption data of the N₂ adsorption isotherm, employing the Brunauer-Emmett-Teller (BET) theory. The pore size distribution was analyzed using the Barrett-Joyner-Halenda (BJH) technique. The chemical states of the materials were determined by X-ray photoelectron spectroscopy (XPS, Thermo Fisher ESCALAB Xi+), which generated X-ray with an energy of 1486.7 eV to identify the valence states of the elements.

2.3. Fabrication and Measurement of the Gas Sensor

15 mg of the as-synthesized CeO₂/CNCs composite were mixed with 1 mL of ethanol to prepare dispersion that were finally deposited on the alumina substrate, and following an ultrasonically dispersing for 30 min. Then, 20 μ L of the solution was dropped onto the Au interdigital electrode and dried at 60 °C overnight, the schematic of the process is illustrated in Figure 1b.

The gas sensing properties were investigated on a dual-channel gas system (BONA TECH BN2914), which obtained the resistance change curve by introducing the mixture gases of test gas and dry air. In particular, the target gas (NO₂) was used to test the sensing performance, and dry air was selected as the carrier gas. Moreover, the effect of humidity on the sensing material can be analysed by adjusting the relative humidity in controlled environment chamber.

The study assessed the performance of the gas sensor under examination through measuring changes in electrical resistance at various concentrations of NO₂ under standard temperature (24 °C). The NO₂ gas concentration test sequence was 10, 20, 30, 50 and 80 ppm, respectively. The percent sensor response (S%) can be calculated by $S = (R_o - R_g) / R_o \times 100$ where, R_o and R_g represent the resistance of the sensor when exposed to dry air and target gas, respectively. The resistance of materials can not completely recover to the initial value in a short time, because of the robust adsorption effect of composites on the target gas. Hence, solely the 5-min response to the initiation of the test gas and the subsequent 5-min recuperation following the discontinuation of the test gas introduction were documented. To guarantee the validity of the followed experiment, the samples were preserved at 60 °C for 12 h before the next test.

3. Results and Discussion

3.1. Morphological and Structural Characteristics

The crystal structures of CeO₂, CNCs, and CeO₂/CNCs were examined by analyzing XRD patterns, as shown in Figure 2. The primary peaks observed in the XRD patterns of CeO₂ and CeO₂/CNCs correspond to a cubic CeO₂ structure (JCPDS, ICDD NO. 34-394), specifically the (111), (200), (220), (311), (222), (400), (331), and (420) planes. Furthermore, the presence of the (002) orientation in the pattern of the CeO₂/CNCs composite confirms the successful synthesis of the complex. Notably, the crystallinity of the CeO₂/CNCs composite is diminished as a result of the polycrystalline amorphous characteristics of CNCs, leading to a lower peak intensity in comparison to pure CeO₂ nanoparticles. In

addition, no other peaks were detected in the XRD patterns, indicating the high purity of the synthesized samples.

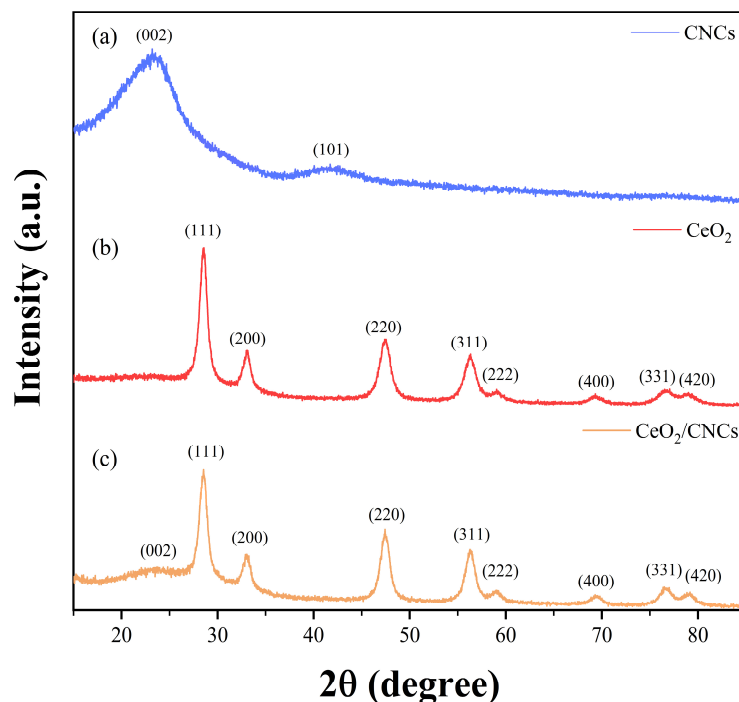


Figure 2. XRD patterns of (a) CNCs, (b) CeO_2 , and (c) CeO_2/CNCs .

The morphology of CeO_2 , CNCs, and CeO_2/CNCs was examined through the utilization of SEM images, as depicted in Figure 3. Figure 3a shows the morphology of the CeO_2 nanoparticles, with the inset providing a magnified view of the agglomerate consisting of several aggregates of CeO_2 nanoparticles. Figure 3b,c display images of the helical structure of CNCs, with the rough surface (as observed in the inset image of Figure 3c) potentially contributing to gas sensing capabilities. The SEM images of CeO_2/CNCs nanocomposite at varying magnifications are presented in Figure 3d–f. A closer look at the SEM image of CeO_2/CNCs composite (Figure 3f) clearly reveals that the CeO_2 nanoparticles are uniformly modified on the surface of the spiral CNCs. The presence of CNCs plays a significant role in preventing agglomeration, particularly when compared to pure CeO_2 . This effect leads to a notable improvement in the contact between the surface of material and the NO_2 gas molecules, ultimately resulting in a noticeable increase in the efficiency of detection.

In order to gain a better understanding of the internal structures of the CNCs, a high-resolution image of their morphology was obtained using TEM, as shown in Figure S1. It is evident from the image that the inner spiral shape of the CNCs consists of a hollow carbon tube structure. This unique structure promotes electron hopping, thereby facilitating the transport of charge carriers. Additionally, the helical arrangement of the CNCs contributes to an increased surface area, which facilitates the adsorption of gas molecules by providing a greater number of adsorption sites. To further investigate the influence of specific surface area on the gas-sensitive properties, porosity analysis was performed on the CNCs and CeO_2/CNCs material using N_2 adsorption-desorption isotherm experiments (Figure S2). The results reveal that both the CNCs and CeO_2/CNCs material exhibit type IV isotherms, with the adsorption hysteresis loop attributed to the presence of ordered mesoporous channels in the materials. The specific surface areas and pore characteristics of the CNCs and CeO_2/CNCs were determined and presented in Table 1. The uncoated CNCs have a specific surface area of $38.8186 \text{ m}^2 \text{ g}^{-1}$ and an average pore size of 8.054 nm , while with a micropore area of $0.000158 \text{ cm}^3 \text{ g}^{-1}$, which restricts the diffusion of gas molecules within the material. In contrast, the CeO_2/CNCs nanocomposite exhibit higher porosity, with a specific surface area of $83.6895 \text{ m}^2 \text{ g}^{-1}$, a micropore area of $0.020243 \text{ cm}^3 \text{ g}^{-1}$, and an

average pore size of 7.2005 nm. These characteristics provide an increasing number of active sites for the interaction with target gases.

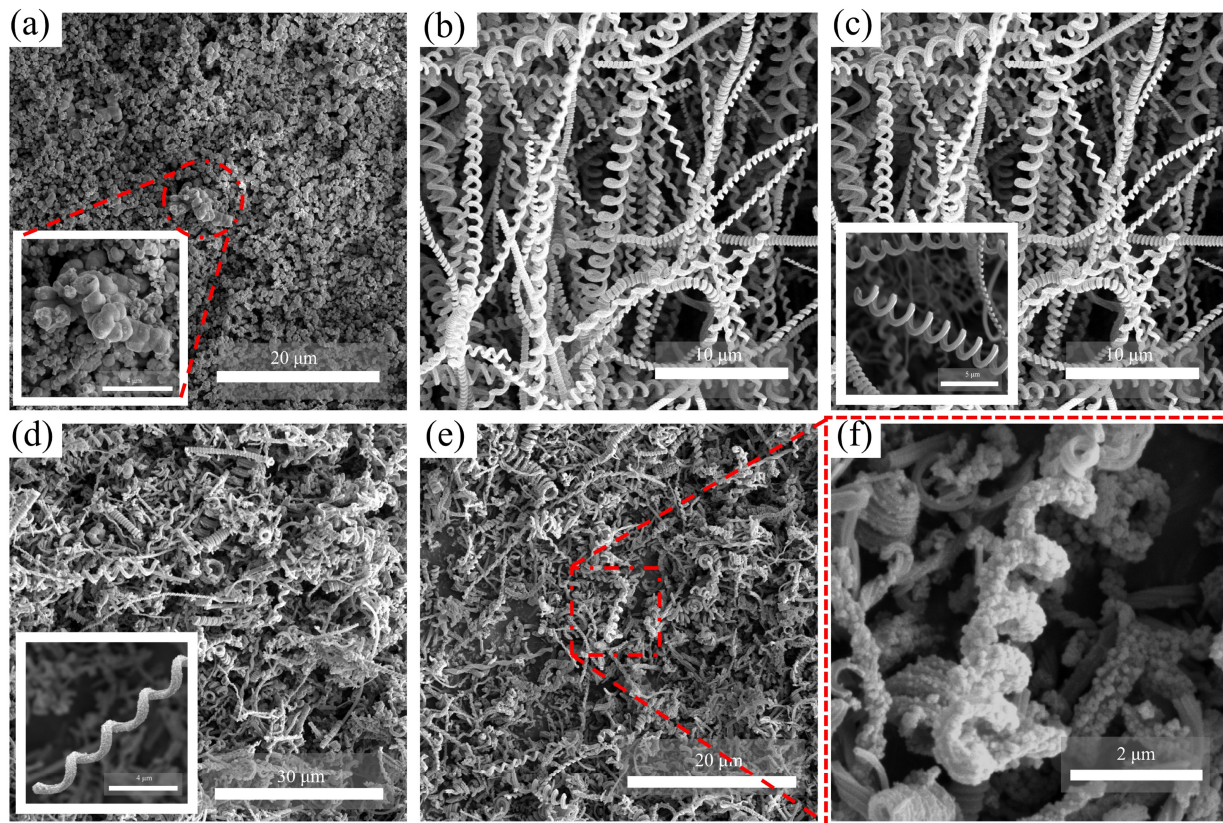


Figure 3. SEM images of (a) CeO₂ nanoparticles (b,c) CNCs and (d–f) CeO₂/CNCs nanocomposite. Insets in a, c and d show the views of the CeO₂ nanoparticles, CNCs and CeO₂/CNCs nanocomposite at higher magnification.

Table 1. The physical properties of as-prepared samples.

Samples	S _{BET} (m ² g ⁻¹)	Micropore Volume (cm ³ g ⁻¹)	Pore Volume (cm ³ g ⁻¹)	Average Pore Size (nm)
CNCs	38.8186	0.000158	0.078161	8.054
CeO ₂ /CNCs	83.6895	0.020243	0.083183	7.2005

3.2. Gas Sensing Properties

The effects of different amounts of CeO₂/CNCs nanocomposites on NO₂ sensing performance were studied, as shown in the Figure 4a–c. It can be clearly seen that the sensitivity increases gradually with the increase in content of Ce within the range of 0.3 to 0.7.

However, the response decreases when the CeO₂ content is further increased. The responses of CeO₂/CNCs-0.3, CeO₂/CNCs-0.5, and CeO₂/CNCs-0.9 samples to 50 ppm concentration of NO₂ are approximately 14.3%, 27.8%, and 29.3%, respectively (see in Figure 4c). When comparing to above samples, the mass ratio of CeO₂/CNCs-0.7 demonstrates superior sensing performance, which exhibits about two to three times greater sensitivity (65.2%) than that of obtained composites. The diminished responsiveness observed in CeO₂/CNCs-0.9 compared to CeO₂/CNCs-0.7 can be attributed to the heightened crystallinity of CeO₂, leading to increased resistance that partially obstructs electron transport within the system, consequently yielding lower response magnitudes. As shown in Figure 4d, the responses of CeO₂/CNCs-0.7 and bare CNCs to varying concentrations of NO₂ (10–80 ppm) reveal that the sensitivity increases with gas concentration. Furthermore, the CeO₂/CNCs composite sample delivers a better sensing performance than bare CNCs. In particular, the response

of CeO₂/CNCs to 30 ppm (47.3) is nearly ten times higher than the response of bare CNCs (4.69). In fact, pure CNCs display low efficiency in detecting NO₂ gas due to its low resistance, which is insufficient to produce significant changes in conductivity. Therefore, the sensing performance can be improved by appropriately increasing the content of CeO₂, and highly sensitive CeO₂/CNCs-0.7 composites are considered potential sensing materials for the following studies.

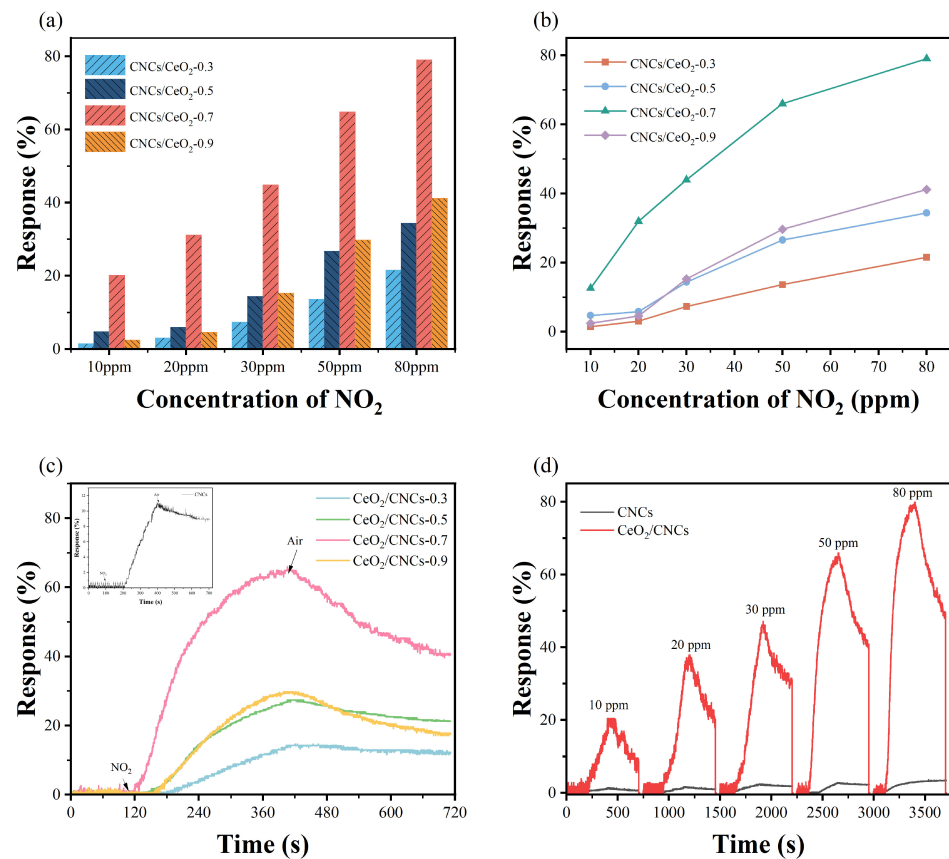


Figure 4. (a,b) The responses of CeO₂/CNC nanocomposite to different concentrations of NO₂. (c) Dynamic response–recovery curves of CeO₂/CNC nanocomposite with different mass ratios of CeO₂ in the presence of 50 ppm NO₂. Insets in c show the dynamic response–recovery curves of pure CNCs. (d) Dynamic response–recovery curves of CNCs and CeO₂/CNCs upon exposure to NO₂ with a concentration range of 10–80 ppm.

The experimental results present the tests of CeO₂/CNCs nanocomposites with the same mass ratio, synthesized at various MWS reaction temperatures, as depicted in Figure 5. Specifically, in Figure 5a–c, it can be observed that sample 3 exhibited more pronounced sensitivity and faster response times in multiple concentration ranges, when compared to the tests conducted on sample 1 and sample 2. Furthermore, the response values and response times for sample 3 were found to be 64.26% and 180 s in the presence of 50 ppm NO₂, which were similar to sample 4 (56.48% and 192 s). Conversely, the response of samples 1 and 2, synthesized at lower temperatures, was only 31.2% and 45.6%, respectively, with response times of 223 s and 235 s. Overall, the sensitivity of the as-prepared samples increased gradually with an increase in reaction temperature, reaching its maximum at approximately 140 °C. It should be noted that excessive temperature can promote the crystallization of additional CeO₂ and, to some extent, limit the efficiency of electron transfer in the material. Additionally, the resistance decreases when an oxidizing gas is passed, indicating that the composites exhibit p-type semiconducting properties. However, the resistance of complexes face difficulty returning to their initial state within a short period of time, because the rapid desorption of NO₂ molecules is hindered as the presence

of van der Waals forces. Typically, the recovery of sample is accelerated by drying in an oven, and eliminates the effects of moisture present in the air.

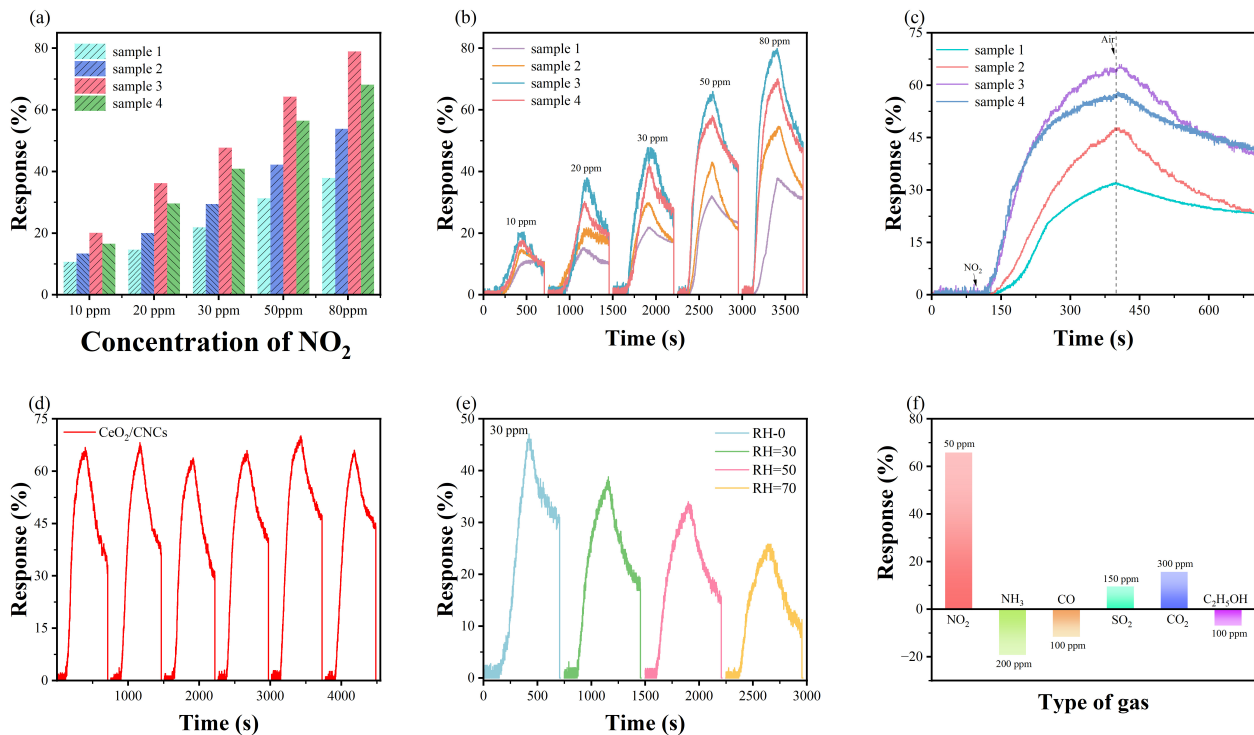


Figure 5. The responses of CeO₂/CNC composites synthesized at various reaction temperatures for (a,b) 10–80 ppm and (c) 50 ppm NO₂. (d) Repeatability of CeO₂/CNCs on cycling exposure to NO₂ in the presence of 50 ppm NO₂. (e) Responses of CeO₂/CNCs to 30 ppm NO₂ with various humidities. (f) Responses of CeO₂/CNCs to different target gases at room temperature.

The limit of detection (LOD) is defined as $3\text{RMS}_{\text{noise}}/\text{slope}$. From the fitting curve (Figure S3), the calculated LOD of CeO₂/CNCs (sample 3) to NO₂ is determined to be 710.3 ppb. A comparison with other NO₂ sensors at room temperature also be presented in Table 2.

Table 2. Comparison of our prepared NO₂ sensor with previously reported other NO₂ sensor.

Material	Method	Concentration (ppm)	Response/Recovery Time (s)	Response	LOD (ppm)	Ref
CeO ₂ /graphene	Hydrothermal	50	30/85	24.82%	-	[32]
NiO/CNCs	Hydrothermal	60	126/-	11.9%	60.3 ppb	[29]
Fe ₃ O ₄ /rGO	Hydrothermal	400	275/738	24.2%	30	[33]
In ₂ O ₃ cubes/rGO	Hydrothermal	5	149/243	37.81%	-	[34]
Co ₃ O ₄ /MWCNT	Hydrothermal	1000	-/-	32%	0.1	[35]
PPy/N-MWCNT	In-situ self-assembly/ annealing	5	65/668	24.82%	-	[36]
ZnO/SWCNTs	MW-irradiation	1	-/-	5.03	88 ppb	[3]
In-SnO ₂ -RGO	Hydrothermal	100	-/-	11	-	[37]
CeO ₂ /CNCs	MWS method	50	180/-	65.4%	710.3 ppb	this work

Furthermore, the multi-cycling properties and gas selectivity are the important parameter for gas sensors. The response degree of composites to 50 ppm NO₂ was tested in six cycling curves, which remained reliable stabilisation in the range of 63.5% to 69.2% (Figure 5d). Moreover, the response degrees of composites to NH₃, CO, SO₂, CO₂ and C₂H₅OH are shown in Figure 5f. It is evident that the sensitivity is much higher when detecting the NO₂, indicating the perfect selectivity of the sensing material at RT. In fact, this selectivity is attributed to the ability of the sensing materials to react with anion oxygen [38]. The defect sites (such as oxygen vacancies and antisite defects) in the composites, as well

as the adsorption capacity and catalytic activity for the target gas, are the main factors contributing to the formation of selectivity [39]. Furthermore, the impact of environmental humidity on the gas sensing characteristics of the CeO₂/CNCs nanocomposite are also examined. Figure 5e displays the responses of composites for 20 ppm NO₂ at different relative humidity (RH), and it is observed that the sensitivity decreases rapidly with the increasing of RH. This is because in humid environments, water molecules are adsorbed on the surface of the sensing material, hindering further contact between the active site and the gas molecules [40]. In addition, water molecules can react with NO₂ molecules to form HNO₃, which impairs the gas sensing response. Therefore, humidity plays a significant role in the gas sensing performance.

3.3. Gas Sensing Mechanism

The utilization of CNCs is significant importance in enhancing the gas sensing performance. To begin with, CNCs have the ability to prevent the aggregation and reformation of CeO₂ nanoparticles. This is because the functionalized CNCs have an abundance of negatively charged oxygen-containing groups, which allows for the adsorption of Ce³⁺ ions through electrostatic interaction. As a result, CeO₂ nanoparticles grow uniformly on the surface of the CNCs during the oxidation reaction [38,41]. This uniform distribution of CeO₂ nanoparticles on helical CNCs creates a large specific surface area, facilitating the permeation and diffusion of target gases within the composites. Additionally, while pure CeO₂ nanoparticles typically exhibit excellent gas sensing performance at high operating temperatures (300 °C) [42], the composite structure benefits from the excellent electrical conductivity and rapid electronic transfer capability of the CNCs. This improvement in electrical properties enhances the ability of gas detection at room temperature. Furthermore, the hybrid structure contains numerous defects, which serve as additional active sites for the adsorption of gases, ultimately enhancing the sensing performance.

3.4. The Effects of Defects on the Gas Sensing Performance

The presence of defects in sensing materials (CeO₂/CNCs) is crucial in enhancing the performance of response by creating numerous vacancies and active sites [43]. The extent of defects can typically be determined through Raman spectroscopy, which quantifies the ratio of the intensity of the D band to the G band, i.e., I_D/I_G. Figure 6a exhibits the results of the Raman measurements conducted on the samples that were prepared. The CNCs, functionalized CNCs, and CeO₂/CNCs composites reveals two graphite-like characteristic peak of D and G band, approximately located at wavenumbers of 1356 cm⁻¹ and 1582 cm⁻¹, respectively. It is acknowledged that the D-band is caused by structural defects and disordered atomic arrangements in sp³ carbon atoms, while the G-band is associated with the E_{2g} vibrational mode in the sp² carbons [23,44]. Moreover, a distinct peak at 458 cm⁻¹ is evident in the spectrum of the CeO₂/CNCs composites, corresponding to the characteristic peak of CeO₂, thereby confirming the successful synthesis of the complex. In addition, the I_D/I_G values of the as-prepared materials were calculated in Figure 6a,b. The characteristic peaks are observed in both CNCs and functionalized CNCs, indicating that the structure remains intact despite oxidation caused by acid treatment. However, the I_D/I_G value for the CNCs increases after functionalization due to the oxidation process, which leads to the destruction of some original bonds and the introduction of new oxygen-containing bonds [45,46]. This increase in the I_D/I_G value can be interpreted as the presence of defects in the structure. Figure 6b illustrates that the I_D/I_G ratio for the CeO₂/CNCs nanocomposites maintains in the range of 1.04 to 1.12, which is close to the values reported for the materials of CeO₂/graphene [32,47,48]. In fact, the gas sensing performance depends heavily on the effect of such defects, and is closely associated with the content of the defect.

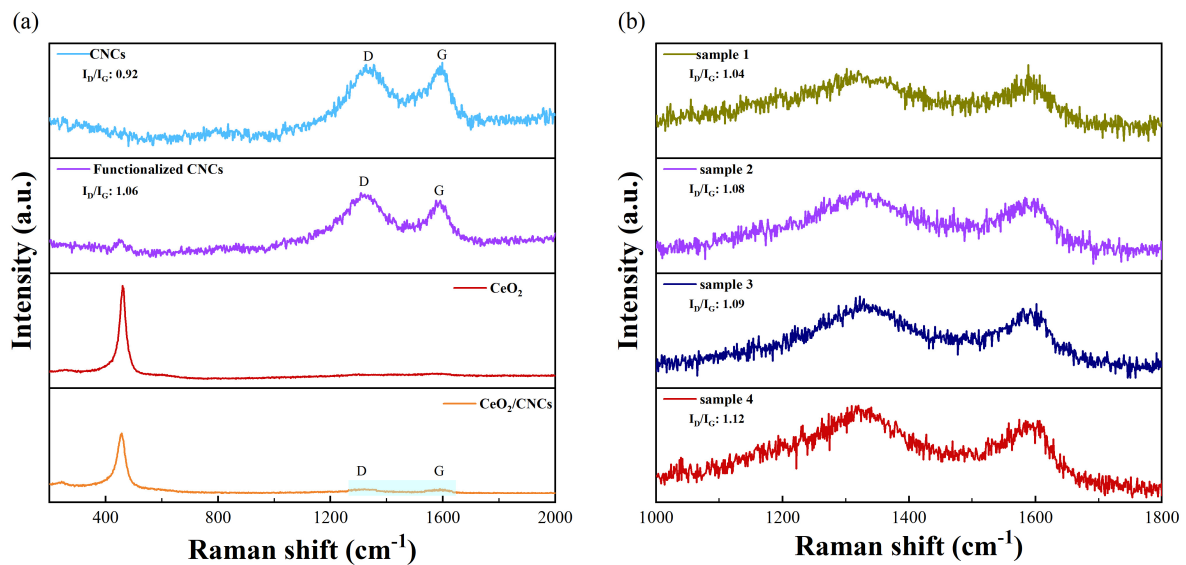


Figure 6. Raman scattering spectra for (a) the CNCs, functionalized CNCs, CeO₂ and CeO₂/CNCs composites; (b) CeO₂/CNCs composites (sample 1, sample 2, sample 3, sample 4) prepared at different temperature.

The crucial role of oxygen vacancy defects in sensing material in promoting the adsorption of gas molecules and facilitating electron transfer by providing more active sites has long been recognized [49]. In this study, the surface compositions and elemental chemical states of the CeO₂/CNCs samples were analyzed using X-ray photoelectron spectroscopy (XPS). By employing X-ray radiation at an energy of 1486.7 eV, one can readily acquire the signals corresponding to the three atoms, namely Carbon (C), Oxygen (O), and Cerium (Ce). The findings present the detailed high-resolution survey spectrum (Figure 7a) alongside the X-ray photoelectron spectra of the sample depicted in Figures 7b–f and 8.

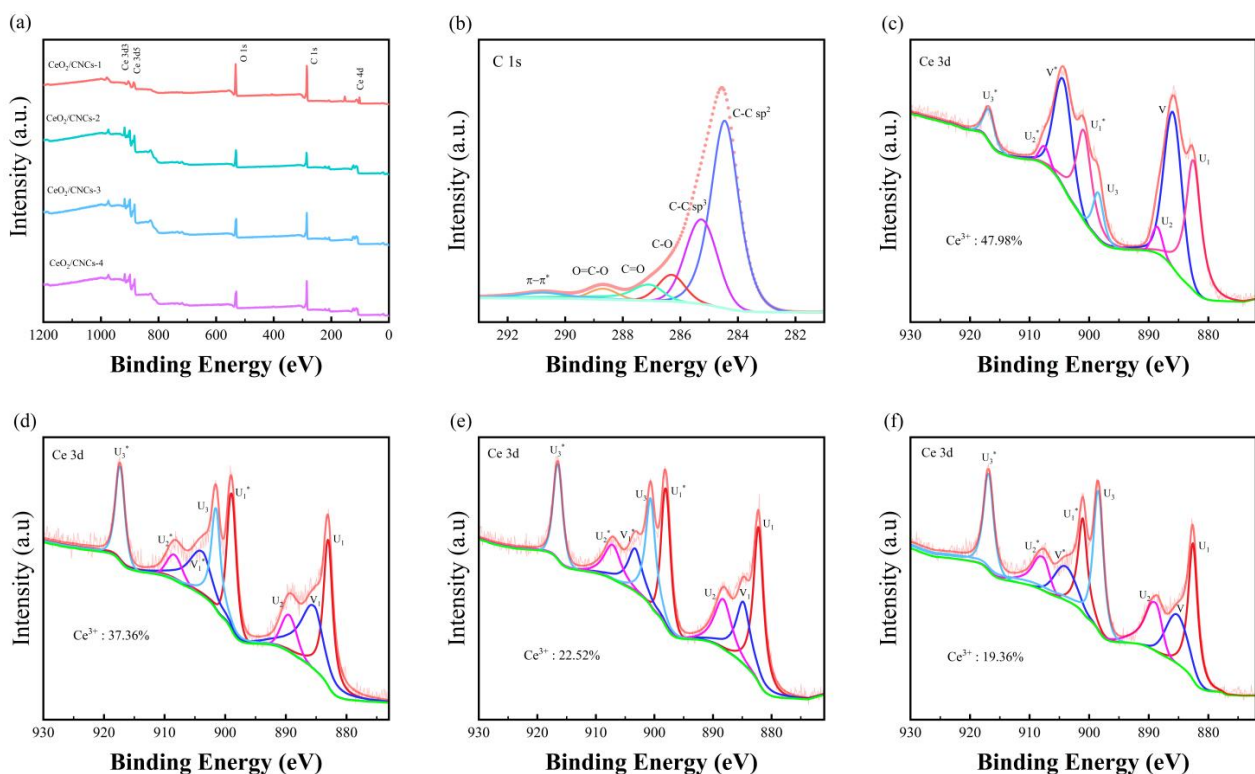


Figure 7. XPS spectra: (a) survey spectra, (b) C 1s and (c–f) Ce 3d of the sample 1, sample 2, sample 3 and sample 4.

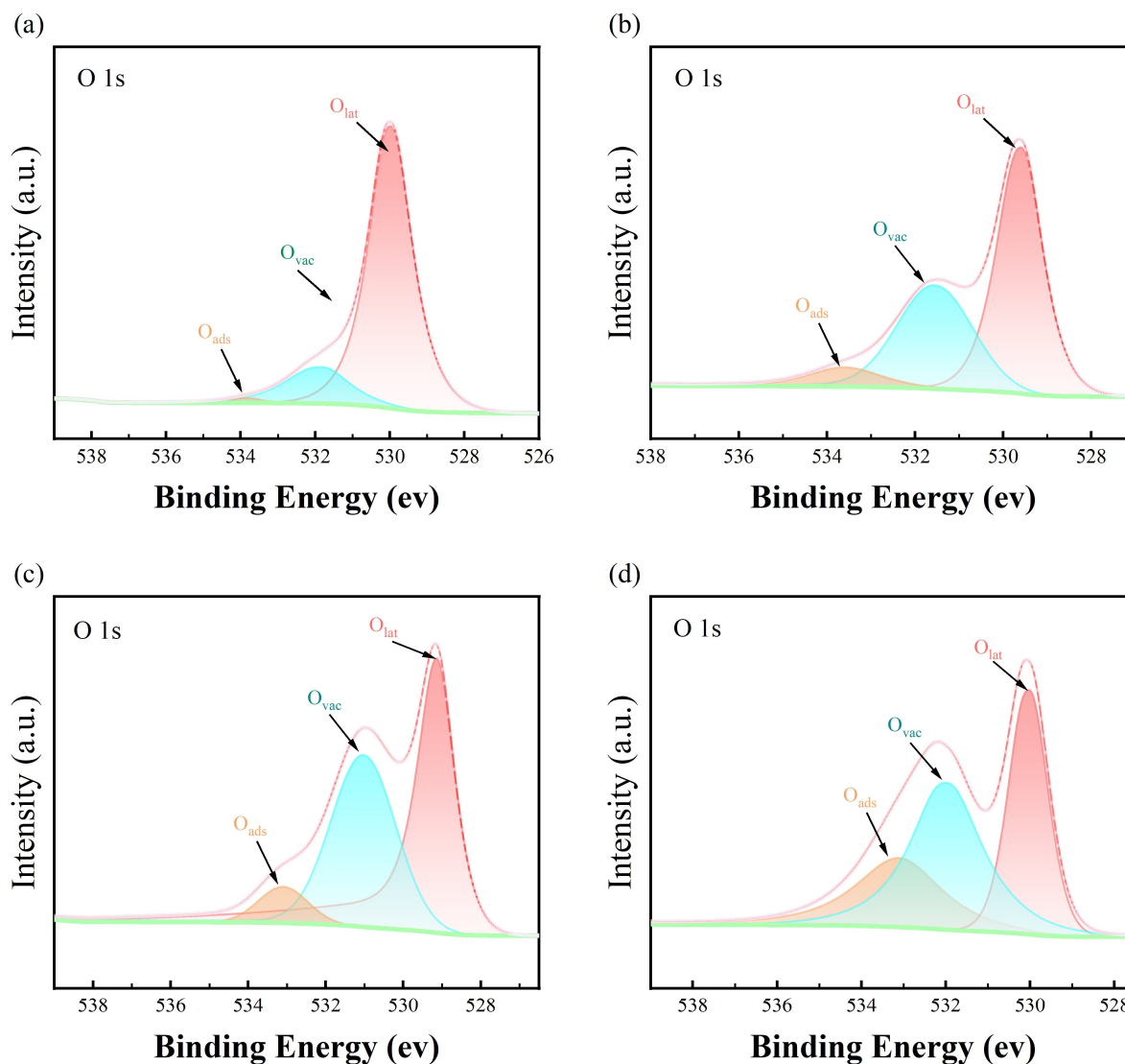
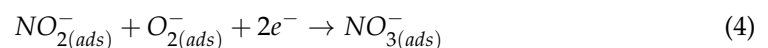


Figure 8. XPS spectrum of O 1s for (a) sample 1, (b) sample 2, (c) sample 3, (d) sample 4.

The survey spectrum of the synthesized CeO_2/CNCs samples displays a complex structure. The three peak groups correspond to the energy intervals of C, Ce, and O elements, with no peaks indicating the presence of other elements, suggesting a high level of purity in the synthesized material, see in Figure 7a. The high-resolution C 1s spectrum of CeO_2/CNCs , as illustrated in Figure 7b, exhibits notable characteristics that are effectively delineated through a fitting utilizing six components. Predominantly featured in the spectrum is a central component positioned at a binding energy of 284.63 eV ($\text{BE} = 284.63 \text{ eV}$) displaying an asymmetrical profile. This constitution is indicative of the sp^2 graphite heterogeneous phase involving carbon-carbon double bonds ($\text{C}=\text{C}$) [25]. Another constituent is situated at higher binding energies relative to the primary peak ($\text{BE} = 285.1 \text{ eV}$) and displays a symmetrical profile. This particular component is distinctly associated with the C-C phase, characterized by sp^3 hybridization of the valence electron states of carbon atoms, which corresponds to the diamond heterostructure under the unique helical structure [50]. The spectral analysis encompasses various chemical bonding configurations involving oxygen, hydrogen, and carbon resulting from the introduction of numerous functional groups through acidification. These constituents primarily consist of C-O (epoxy and hydroxyl), C=O (carbonyl), and O-C=O (carboxyl) bond categories [51–53], each exhibiting binding energies of 286.42 eV, 287.44 eV, and 288.32 eV, respectively. The energy binding peak located at 290.5 eV is assigned to $\pi-\pi^*$ shakeup satellite. The XPS

spectra of Ce 3d in the CeO₂/CNCs composites revealed six binding energy peaks (U_1 , U_2 , U_3 , U_1^* , U_2^* and U_3^*) attributed to Ce 3d_{5/2} and 3d_{3/2} of Ce⁴⁺ ions, as well as V and V* peaks corresponding to Ce 3d_{5/2} and 3d_{3/2} of Ce³⁺ ions, seen in Figure 7c–f. To further investigate the surface oxygen states, the O 1s spectra of the samples were analyzed and divided into three peaks representing O_{lat} (latticeoxygen), O_{vac} (oxygenvacancies) and O_{ads} (chemisorbed oxygen species), as shown in Figure 8a–d. O_{lat} with the binding energy in the range of 529.2–530.4 eV represents oxygen ions in the crystal lattice, which does not contribute to the gas response. O_{vac} and O_{ads}, with the binding energies of approximately 531.5 eV and 533.7 eV, play an important role in improving gas sensitivity [38,54,55]. According to the relative area of the fitted peaks, the ratios of cerium and oxygen are listed in Table S1. It is observed that at lower reaction temperatures, the dominant species are Ce³⁺ ions and lattice oxygen. However, as the synthesis temperature is increased from 100 to 140 °C, the concentration of Ce³⁺ decreases from 47.98 to 19.38%, while the concentration of O_{lat} decreases from 84.6 to 53.02%. This decrease in Ce³⁺ ions is attributed to their transformation into Ce⁴⁺ under high heat, while the lattice oxygen evolves into oxygen vacancy defects and chemisorbed oxygen. Among these samples, sample 3 synthesized at 140 °C exhibits the highest concentration of O_{vac} at 35.6%. The concentration of O_{vac} slightly decreases to 34.69% when the temperature is further increased to 160 °C (sample 4). While tested at 50 ppm, shows a decrease in response degree of 56.4%, which is smaller compared to sample 3 (65.3%) due to electron transfer barriers during the recrystallization of CeO₂. These results highlight the significant role of oxygen vacancies and chemisorbed oxygen in gas sensing. Moreover, the content of these components can be adjusted by manipulating the reaction temperature, which in turn enhances the sensing performance.

The gas sensing mechanism portrayed in Figure 9 can be described as follows during a dynamic process. Upon exposure to air, oxygen molecules will be adsorbed onto the oxygen vacancies inherent in the sensing material. These oxygen molecules then capture unbound electrons from the conduction band or donor energy level of the composites, resulting in the formation of O₂[−]. This notably augments the adsorption of oxygen in the materials, thereby facilitating the movement of electrons across the interface. Consequently, an additional electron depletion layer is formed and a Schottky contact is established. In simpler terms, the consumption of electrons is tantamount to the generation of an equal number of holes, which culminates in the development of a hole accumulation layer (HAL) on the surface of material (as shown in Figure 9b). When exposed to NO₂, the interaction between NO₂ molecules and the surface oxygen species leads to further electron capture on the conduction band of the composites, resulting in a thicker HAL (Figure 9c). Since holes serve as the conducting carriers in p-type semiconductors, this precipitates a sudden and significant decline in resistance. The specific formulae describing this phenomenon are outlined as follows:



In addition, cerium oxide exhibits the ability to release lattice oxygen under hypoxic conditions. This process leads to the transformation of Ce⁴⁺ ions into Ce³⁺ and the formation of extra oxygen vacancy defects [56,57]. Consequently, the concentration of oxygen vacancy defects in the composites is increased, thereby promoting the adsorption and ionization of oxygen on the material. Hence, it is evident that the combined influence of Ce⁴⁺ ions and oxygen vacancy defects greatly enhance the capacity of material to adsorb NO₂ gas, thereby improving its gas-sensitive performance.



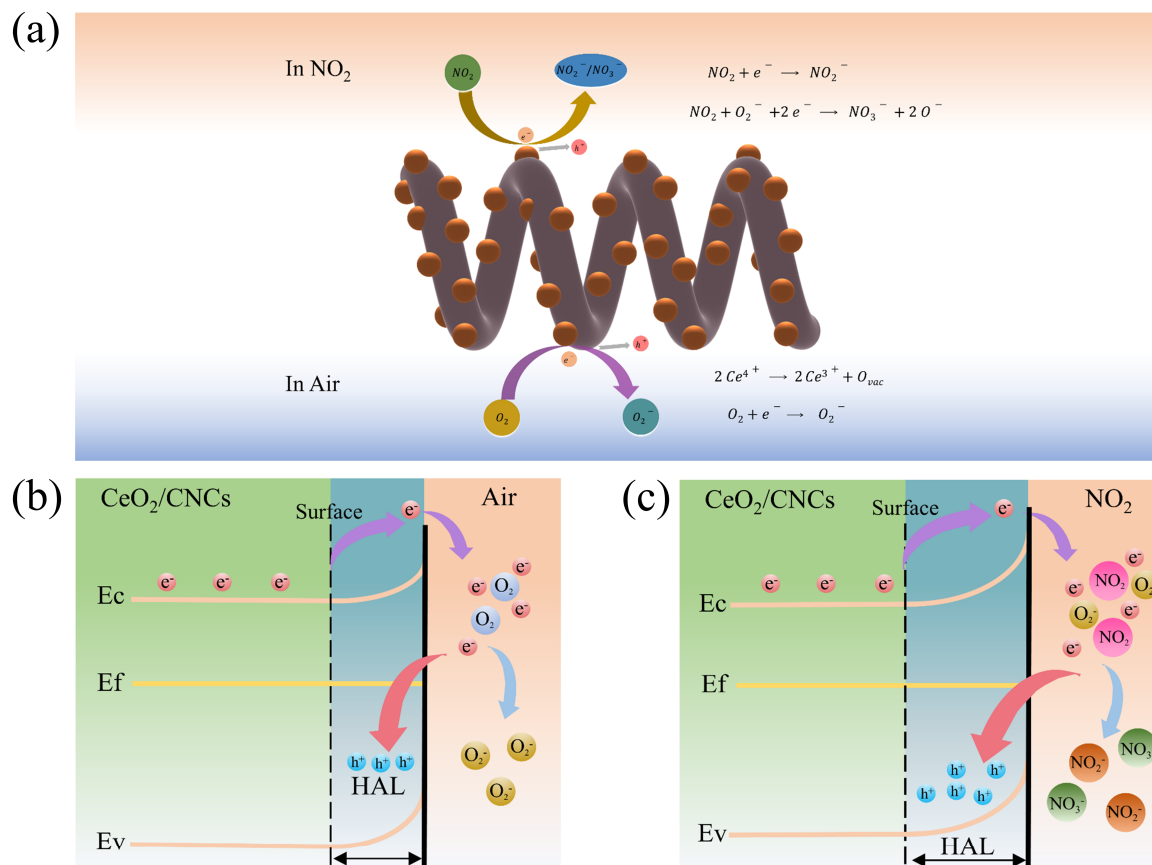


Figure 9. (a) Schematic for the gas-sensing mechanism; The adsorption sensing mechanism on the surface of CeO₂/CNCs composites for (b) O₂ and (c) NO₂.

4. Conclusions

In this work, CeO₂/CNCs nanocomposites were successfully synthesized using a microwave-solvothermal method, in which uniformly assembled CeO₂ nanoparticles on the surface of CNCs. The microstructures and compositions of the resulting composites were analysed using various characterization techniques and gas-sensing tests. The nanocomposite doped with the mass of Ce precursors (0.7) demonstrated the highest sensitivity, with a response of 65.4 to 60 ppm NO₂ at room temperature. This sensitivity was nearly 9 times greater than that observed with bare CNCs. Furthermore, the gas sensing properties of the composites could be indirectly modulated by adjusting the appropriate reaction temperature to increase the oxygen vacancy defects. Overall, the microwave-solvothermal method offers a simple approach for designing and synthesizing nanocomposites with unique physicochemical properties, making them suitable for smart applications.

Supplementary Materials: The following supporting information can be downloaded at: <https://www.mdpi.com/article/10.3390/nano14100812/s1>, Figure S1: TEM image of CNCs; Figure S2: The N₂ adsorption and desorption isotherms and pore size distribution (the inset) curve of bare CNCs (a) and (b) CeO₂/CNCs nanocomposite; Figure S3: Fitting curve of the CeO₂/CNCs composites. Table S1: The ratios of cerium and oxygen of as-prepared samples; ref. [58].

Author Contributions: Conceptualization, Y.S.; methodology, Y.S. and X.L.; validation, Y.S.; formal analysis, Y.H.; investigation, X.L.; resources, Y.H.; data curation, X.L.; writing—original draft preparation, Y.S. and X.L.; writing—review and editing, Y.S. and X.L.; supervision, G.W. and Y.S.; project administration, G.W. and Y.S.; funding acquisition, G.W. and Y.S. All authors have read and agreed to the published version of the manuscript.

Funding: This research was funded by the National Natural Science Foundation of China (NSFC), Grant Nos. 12374355 and 12304425, the Key Project of the National Key R&D Program of China, Grant No. 2022YFA1404500. The APC was funded by the National Natural Science Foundation of China. The authors also wish to acknowledge the assistance on HRTEM observation received from the Electron Microscope Center of Shenzhen University.

Data Availability Statement: Data that support the findings of this study are available from the corresponding author upon reasonable request.

Acknowledgments: The authors acknowledge assistance regarding HRTEM observation received from the Electron Microscope Center of Shenzhen University.

Conflicts of Interest: The authors declare no conflicts of interest.

References

1. Guarnieri, M.; Balmes, J.R. Outdoor air pollution and asthma. *Lancet* **2014**, *383*, 1581–1592. [[CrossRef](#)] [[PubMed](#)]
2. Tobaldi, D.M.; Dvoranová, D.; Lajaunie, L.; Rozman, N.; Figueiredo, B.; Seabra, M.P.; Skapin, A.S.; Calvino, J.J.; Brezová, V.; Labrincha, J.A. Graphene-TiO₂ hybrids for photocatalytic aided removal of VOCs and nitrogen oxides from outdoor environment. *Chem. Eng. J.* **2021**, *405*, 126651. [[CrossRef](#)] [[PubMed](#)]
3. Park, S.; Byoun, Y.; Kang, H.; Song, Y.J.; Choi, S.W. ZnO Nanocluster-Functionalized Single-Walled Carbon Nanotubes Synthesized by Microwave Irradiation for Highly Sensitive NO₂ Detection at Room Temperature. *ACS Omega* **2019**, *4*, 10677–10686. [[CrossRef](#)] [[PubMed](#)]
4. Neri, G. First Fifty Years of Chemosensitive Gas Sensors. *Chemosensors* **2015**, *3*, 1–20. [[CrossRef](#)]
5. Lin, T.T.; Lv, X.; Hu, Z.N.; Xu, A.S.; Feng, C.H. Semiconductor Metal Oxides as Chemosensitive Sensors for Detecting Volatile Organic Compounds. *Sensors* **2019**, *19*, 19020233. [[CrossRef](#)] [[PubMed](#)]
6. Zhang, B.; Cheng, M.; Liu, G.; Gao, Y.; Zhao, L.; Li, S.; Wang, Y.; Liu, F.; Liang, X.; Zhang, T.; et al. Room temperature NO₂ gas sensor based on porous Co₃O₄ slices/reduced graphene oxide hybrid. *Sens. Actuators B Chem.* **2018**, *263*, 387–399. [[CrossRef](#)]
7. Chethana, D.M.; Thanuja, T.C.; Mahesh, H.M.; Kiruba, M.S.; Jose, A.S.; Barshilia, H.C.; Manjanna, J. Synthesis, structural, magnetic and NO₂ gas sensing property of CuO nanoparticles. *Ceram. Int.* **2021**, *47*, 10381–10387. [[CrossRef](#)]
8. Zhang, J.; Zeng, D.W.; Zhu, Q.; Wu, J.J.; Huang, Q.W.; Xie, C.S. Effect of Nickel Vacancies on the Room-Temperature NO₂ Sensing Properties of Mesoporous NiO Nanosheets. *J. Phys. Chem. C* **2016**, *120*, 3936–3945. [[CrossRef](#)]
9. Choi, M.S.; Kim, M.Y.; Mirzaei, A.; Kim, H.S.; Kim, S.I.; Baek, S.H.; Chun, D.W.; Jin, C.H.; Lee, K.H. Selective, sensitive, and stable NO₂ gas sensor based on porous ZnO nanosheets. *Appl. Surf. Sci.* **2021**, *568*, 150910. [[CrossRef](#)]
10. Saruhan, B.; Yüce, A.; Gönüllü, Y.; Kelm, K. Effect of Al doping on NO₂ gas sensing of TiO₂ at elevated temperatures. *Sens. Actuators B Chem.* **2013**, *187*, 586–597. [[CrossRef](#)]
11. Mattmann, M.; Helbling, T.; Durrer, L.; Roman, C.; Hierold, C.; Pohle, R.; Fleischer, M. Sub-ppm NO₂ detection by Al₂O₃ contact passivated carbon nanotube field effect transistors. *Appl. Phys. Lett.* **2009**, *94*, 3125259. [[CrossRef](#)]
12. Nallappan, M.; Gopalan, M. Fabrication of CeO₂/PANI composites for high energy density supercapacitors. *Mater. Res. Bull.* **2018**, *106*, 357–364. [[CrossRef](#)]
13. Slusser, P.; Kumar, D.; Tiwari, A. Unexpected magnetic behavior of Cu-doped CeO₂. *Appl. Phys. Lett.* **2010**, *96*, 3383238. [[CrossRef](#)]
14. Fan, Z.H.; Meng, F.M.; Gong, J.F.; Li, H.J.; Hua, Y.D.; Liu, D.R. Enhanced photocatalytic activity of hierarchical flower-like CeO₂/TiO₂ heterostructures. *Mater. Lett.* **2016**, *175*, 36–39. [[CrossRef](#)]
15. Oosthuizen, D.N.; Motaung, D.E.; Swart, H.C. Gas sensors based on CeO₂ nanoparticles prepared by chemical precipitation method and their temperature-dependent selectivity towards H₂S and NO₂ gases. *Appl. Surf. Sci.* **2020**, *505*, 144356. [[CrossRef](#)]
16. Joy, N.A.; Nandasiri, M.I.; Rogers, P.H.; Jiang, W.L.; Varga, T.; Kuchibhatla, S.; Thevuthasan, S.; Carpenter, M.A. Selective Plasmonic Gas Sensing: H₂, NO₂, and CO Spectral Discrimination by a Single Au-CeO₂ Nanocomposite Film. *Anal. Chem.* **2012**, *84*, 5025–5034. [[CrossRef](#)] [[PubMed](#)]
17. Fang, H.; Shang, E.; Wang, D.; Ma, X.; Zhao, B.; Han, C.; Zheng, C. A chemiresistive ppt level NO₂ gas sensor based on CeO₂ nanoparticles modified CuO nanosheets operated at 100 °C. *Sens. Actuators B Chem.* **2023**, *393*, 134277. [[CrossRef](#)]
18. Young, S.J.; Lin, Z.D. Ammonia gas sensors with Au-decorated carbon nanotubes. *Microsyst. Technol.* **2018**, *24*, 4207–4210.
19. Guo, S.Y.; Hou, P.X.; Zhang, F.; Liu, C.; Cheng, H.M. Gas Sensors Based on Single-Wall Carbon Nanotubes. *Molecules* **2022**, *27*, 27175381. [[CrossRef](#)] [[PubMed](#)]
20. Llobet, E. Gas sensors using carbon nanomaterials: A review. *Sens. Actuators B Chem.* **2013**, *179*, 32–45. [[CrossRef](#)]
21. Rabchinskii, M.K.; Sysoev, V.V.; Glukhova, O.E.; Brzhezinskaya, M.; Stolyarova, D.Y.; Varezchnikov, A.S.; Solomatin, M.A.; Barkov, P.V.; Kirilenko, D.A.; Pavlov, S.I.; et al. Guiding Graphene Derivatization for the On-Chip Multisensor Arrays: From the Synthesis to the Theoretical Background. *Adv. Mater. Technol.* **2022**, *7*, 202101250. [[CrossRef](#)]
22. Liu, Z.Y.; Yu, L.M.; Guo, F.; Liu, S.; Qi, L.J.; Shan, M.Y.; Fan, X.H. Facial development of high performance room temperature NO₂ gas sensors based on ZnO nanowalls decorated rGO nanosheets. *Appl. Surf. Sci.* **2017**, *423*, 721–727. [[CrossRef](#)]
23. Deng, C.H.; Sun, Y.M.; Pan, L.J.; Wang, T.Y.; Xie, Y.S.; Liu, J.; Zhu, B.W.; Wang, X.W. Thermal Diffusivity of a Single Carbon Nanocoil: Uncovering the Correlation with Temperature and Domain Size. *ACS Nano* **2016**, *10*, 9710–9719. [[CrossRef](#)] [[PubMed](#)]

24. Sun, Y.M.; Wang, C.W.; Pan, L.J.; Fu, X.; Yin, P.H.; Zou, H.L. Electrical conductivity of single polycrystalline-amorphous carbon nanocoils. *Carbon* **2016**, *98*, 285–290. [[CrossRef](#)]
25. Zhao, Q.; Pan, L.J.; Ma, H.; Wang, T. Structure changes of an individual carbon nanocoil and its field-emission enhancement by laser treatment. *Diam. Relat. Mater.* **2012**, *22*, 33–36. [[CrossRef](#)]
26. Zuo, X.Q.; Zhao, Y.P.; Zhang, H.; Huang, H.; Zhou, C.; Cong, T.Z.; Muhammad, J.; Yang, X.; Zhang, Y.F.; Fan, Z.; et al. Surface modification of helical carbon nanocoil (CNC) with N-doped and Co-anchored carbon layer for efficient microwave absorption. *J. Colloid Interface Sci.* **2022**, *608*, 1894–1907. [[CrossRef](#)] [[PubMed](#)]
27. Wu, J.; Sun, Y.M.; Wu, Z.X.; Li, X.; Wang, N.; Tao, K.; Wang, G.P. Carbon Nanocoil-Based Fast-Response and Flexible Humidity Sensor for Multifunctional Applications. *ACS Appl. Mater. Interfaces* **2019**, *11*, 4242–4251. [[CrossRef](#)] [[PubMed](#)]
28. Sun, Y.M.; Dong, Z.; Ding, Z.Z.; Wang, N.; Sun, L.; Wei, H.M.; Wang, G.P. Carbon Nanocoils and Polyvinyl Alcohol Composite Films for Fiber-Optic Fabry-Perot Acoustic Sensors. *Coatings* **2022**, *12*, 12101599. [[CrossRef](#)]
29. Sun, Y.M.; Ding, Z.Z.; Zhang, Y.P.; Dong, Z.; Sun, L.; Wang, N.; Yin, M.J.; Zhang, J.; Wang, G.P. Carbon nanocoils decorated with scale-like mesoporous NiO nanosheets for ultrasensitive room temperature ppb-level NO₂ sensing. *Phys. Chem. Chem. Phys.* **2023**, *25*, 3485–3493. [[CrossRef](#)] [[PubMed](#)]
30. Li, Y.; Lu, Y.L.; Wu, K.D.; Zhang, D.Z.; Debliquy, M.; Zhang, C. Microwave-assisted hydrothermal synthesis of copper oxide-based gas-sensitive nanostructures. *Rare Met.* **2021**, *40*, 1477–1493. [[CrossRef](#)]
31. Gao, Y.W.; Chen, D.L.; Hou, X.H.; Zhang, Y.; Yi, S.S.; Ji, H.P.; Wang, Y.; Yin, L.; Sun, J. Microwave-assisted synthesis of hierarchically porous Co₃O₄/rGO nanocomposite for low-temperature acetone detection. *J. Colloid Interface Sci.* **2021**, *594*, 690–701. [[CrossRef](#)] [[PubMed](#)]
32. Zhang, L.Z.; Fang, Q.L.; Huang, Y.H.; Xu, K.W.; Ma, F.; Chu, P.K. Facet-engineered CeO₂/graphene composites for enhanced NO₂ gas-sensing. *J. Mater. Chem. C* **2017**, *5*, 6973–6981. [[CrossRef](#)]
33. Liu, X.; Li, J.W.; Sun, J.B.; Zhang, X.T. 3D Fe₃O₄ nanoparticle/graphene aerogel for NO₂ sensing at room temperature. *Rsc Adv.* **2015**, *5*, 73699–73704. [[CrossRef](#)]
34. Yang, W.; Wan, P.; Zhou, X.D.; Hu, J.M.; Guan, Y.F.; Feng, L. Additive-Free Synthesis of In₂O₃ Cubes Embedded into Graphene Sheets and Their Enhanced NO₂ Sensing Performance at Room Temperature. *ACS Appl. Mater. Interfaces* **2014**, *6*, 21093–21100. [[CrossRef](#)] [[PubMed](#)]
35. Rui, K.; Wang, X.S.; Du, M.; Zhang, Y.; Wang, Q.Q.; Ma, Z.Y.; Zhang, Q.; Li, D.S.; Huang, X.; Sun, G.Z.; et al. Dual-Function Metal-Organic Framework-Based Wearable Fibers for Gas Probing and Energy Storage. *ACS Appl. Mater. Interfaces* **2018**, *10*, 2837–2842. [[CrossRef](#)] [[PubMed](#)]
36. Liu, B.H.; Liu, X.Y.; Yuan, Z.; Jiang, Y.D.; Su, Y.J.; Ma, J.Y.; Tai, H.L. A flexible NO₂ gas sensor based on polypyrrole/nitrogen-doped multiwall carbon nanotube operating at room temperature. *Sens. Actuators B Chem.* **2019**, *295*, 86–92. [[CrossRef](#)]
37. Cui, S.M.; Wen, Z.H.; Mattson, E.C.; Mao, S.; Chang, J.B.; Weinert, M.; Hirschmugl, C.J.; Gajdardziska-Josifovska, M.; Chen, J.H. Indium-doped SnO₂ nanoparticle-graphene nanohybrids: Simple one-pot synthesis and their selective detection of NO₂. *J. Mater. Chem. A* **2013**, *1*, 4462–4467. [[CrossRef](#)]
38. Zhang, L.Z.; Fang, Q.L.; Huang, Y.H.; Xu, K.W.; Chu, P.K.; Ma, F. Oxygen Vacancy Enhanced Gas-Sensing Performance of CeO₂/Graphene Heterostructure at Room Temperature. *Anal. Chem.* **2018**, *90*, 9821–9829. [[CrossRef](#)] [[PubMed](#)]
39. Li, L.; He, S.J.; Liu, M.M.; Zhang, C.M.; Chen, W. Three-Dimensional Mesoporous Graphene Aerogel-Supported SnO₂ Nanocrystals for High-Performance NO₂ Gas Sensing at Low Temperature. *Anal. Chem.* **2015**, *87*, 1638–1645. [[CrossRef](#)] [[PubMed](#)]
40. Wang, C.X.; Yin, L.W.; Zhang, L.Y.; Xiang, D.; Gao, R. Metal Oxide Gas Sensors: Sensitivity and Influencing Factors. *Sensors* **2010**, *10*, 2088–2106. [[CrossRef](#)] [[PubMed](#)]
41. Jiang, X.X.; Tai, H.L.; Ye, Z.B.; Yuan, Z.; Liu, C.H.; Su, Y.J.; Jiang, Y.D. Novel p-n heterojunction-type rGO/CeO₂ bilayer membrane for room-temperature nitrogen dioxide detection. *Mater. Lett.* **2017**, *186*, 49–52. [[CrossRef](#)]
42. Bi, H.; Zhang, L.X.; Xing, Y.; Zhang, P.; Chen, J.J.; Yin, J.; Bie, L.J. Morphology-controlled synthesis of CeO₂ nanocrystals and their facet-dependent gas sensing properties. *Sens. Actuators B Chem.* **2021**, *330*, 129374. [[CrossRef](#)]
43. Molina, A.; Al-Sardar, M.; Rodriguez-Gonzalez, V.; Escobar-Barrios, V.; Zakhidov, A.A.; Mtz-Enriquez, A.I.; Encinas, A.; Oliva, J. Efficient NO₂ detection and the sensing mechanism of stretchable/ biodegradable MWCNT based sensors decorated with CeO₂ nanoparticles. *Synth. Met.* **2022**, *287*, 117091. [[CrossRef](#)]
44. Khan, A.S.; Pan, L.J.; Farid, A.; Javid, M.; Huang, H.; Zhao, Y.P. Carbon nanocoils decorated with a porous NiCo₂O₄ nanosheet array as a highly efficient electrode for supercapacitors. *Nanoscale* **2021**, *13*, 11943–11952. [[CrossRef](#)] [[PubMed](#)]
45. Osorio, A.G.; Silveira, I.C.L.; Bueno, V.L.; Bergmann, C.P. H₂SO₄/HNO₃/HCl-Functionalization and its effect on dispersion of carbon nanotubes in aqueous media. *Appl. Surf. Sci.* **2008**, *255*, 2485–2489. [[CrossRef](#)]
46. Mittal, M.; Kumar, A. Carbon nanotube (CNT) gas sensors for emissions from fossil fuel burning. *Sens. Actuators B Chem.* **2014**, *203*, 349–362. [[CrossRef](#)]
47. Ji, Z.Y.; Shen, X.P.; Li, M.Z.; Zhou, H.; Zhu, G.X.; Chen, K.M. Synthesis of reduced graphene oxide/CeO₂ nanocomposites and their photocatalytic properties. *Nanotechnology* **2013**, *24*, 115603. [[CrossRef](#)] [[PubMed](#)]
48. Takte, M.A.; Ingle, N.N.; Dole, B.N.; Tsai, M.L.; Hianik, T.; Shirsat, M.D. A stable and highly-sensitive flexible gas sensor based on Ceria (CeO₂) nano-cube decorated rGO nanosheets for selective detection of NO₂ at room temperature. *Synth. Met.* **2023**, *297*, 117411. [[CrossRef](#)]

49. Liu, H.L.; He, H.L.; Chen, L.Q.; Pan, Q.J.; Zhang, G. Flower-like Co_3O_4 sensor with rich oxygen vacancy defects for enhancing room temperature NO_x sensing performances. *J. Alloys Compd.* **2021**, *868*, 159180. [[CrossRef](#)]
50. Liu, L.Z.; Gao, H.L.; Zhao, J.J.; Lu, J.P. Quantum conductance of armchair carbon nanocoils: Roles of geometry effects. *Sci. China-Phys. Mech. Astron.* **2011**, *54*, 841–845. [[CrossRef](#)]
51. Sobaszek, M.; Brzhezinskaya, M.; Olejnik, A.; Mortet, V.; Alam, M.; Sawczak, M.; Ficek, M.; Gazda, M.; Weiss, Z.; Bogdanowicz, R. Highly Occupied Surface States at Deuterium-Grown Boron-Doped Diamond Interfaces for Efficient Photoelectrochemistry. *Small* **2023**, *19*, 202208265. [[CrossRef](#)]
52. Brzhezinskaya, M.; Bauman, Y.I.; Maksimova, T.A.; Stoyanovskii, V.O.; Vedyagin, A.A.; Mishakov, I.V.; Shubin, Y.V.; Gerasimov, E.Y. One-pot functionalization of catalytically derived carbon nanostructures with heteroatoms for toxic-free environment. *Appl. Surf. Sci.* **2022**, *590*, 153055. [[CrossRef](#)]
53. Brzhezinskaya, M.; Belenkov, E.A.; Greshnyakov, V.A.; Yalovega, G.E.; Bashkin, I.O. New aspects in the study of carbon-hydrogen interaction in hydrogenated carbon nanotubes for energy storage applications. *J. Alloys Compd.* **2019**, *792*, 713–720. [[CrossRef](#)]
54. Sun, K.; Zhan, G.H.; Zhang, L.; Wang, Z.L.; Lin, S.W. Highly sensitive NO_2 gas sensor based on ZnO nanoarray modulated by oxygen vacancy with Ce doping. *Sens. Actuators B Chem.* **2023**, *379*, 133294. [[CrossRef](#)]
55. Wang, X.; Wang, T.K.; Si, G.K.; Li, Y.; Zhang, S.W.; Deng, X.L.; Xu, X.J. Oxygen vacancy defects engineering on Ce-doped $\alpha\text{-Fe}_2\text{O}_3$ gas sensor for reducing gases. *Sens. Actuators B Chem.* **2020**, *302*, 127165. [[CrossRef](#)]
56. Chen, J.J.; Zhou, N.; Wang, H.Y.; Peng, Z.G.; Li, H.Y.; Tang, Y.G.; Liu, K. Synergistically enhanced oxygen reduction activity of $\text{MnO}_x\text{-CeO}_2/\text{Ketjenblack}$ composites. *Chem. Commun.* **2015**, *51*, 10123. [[CrossRef](#)]
57. Hu, J.; Sun, Y.J.; Xue, Y.; Zhang, M.; Li, P.W.; Lian, K.; Zhuiykov, S.; Zhang, W.D.; Chen, Y. Highly sensitive and ultra-fast gas sensor based on CeO_2 -loaded In_2O_3 hollow spheres for ppb-level hydrogen detection. *Sens. Actuators B Chem.* **2018**, *257*, 124–135. [[CrossRef](#)]
58. Duy, L.T.; Kim, D.J.; Trung, T.Q.; Dang, V.Q.; Kim, B.Y.; Moon, H.K.; Lee, N.E. High Performance Three-Dimensional Chemical Sensor Platform Using Reduced Graphene Oxide Formed on High Aspect-Ratio Micro-Pillars. *Adv. Funct. Mater.* **2015**, *25*, 883–890. [[CrossRef](#)]

Disclaimer/Publisher’s Note: The statements, opinions and data contained in all publications are solely those of the individual author(s) and contributor(s) and not of MDPI and/or the editor(s). MDPI and/or the editor(s) disclaim responsibility for any injury to people or property resulting from any ideas, methods, instructions or products referred to in the content.